Probing the Electronic Band Structure of Emerging Chalcogenide Absorbers for Photoelectrochemistry

Beatriz de la Fuente[1‡], Daniely Reis Santos[2,3,4‡], Irene Dei Tos[2,3,4], Bart Ruttens[2], Jan D'Haen[2], Sudhanshu Shukla[2,3,4], Bart Vermang[2,3,4], Juliet Risner-Jamtgaard[5], Annick Hubin[1], Tom Hauffman[1]*

[1]*Research group Sustainable Materials Engineering (SUME), Lab of Electrochemical and Surface Engineering (SURF), Vrije Universiteit Brussel, Pleinlaan 2, Brussels 1050, Belgium*

[2]*Hasselt University, Institute for Materials Research, Imo-imomec, Martelarenlaan 42, 3500 Hasselt, Belgium*

[3]*Imec, Imo-imomec, Thor Park 8320, 3600 Genk, Belgium*

[4]*EnergyVille, Imo-imomec, Thor Park 8320, 3600 Genk, Belgium*

[5]*SNSF, Stanford University, Stanford, California 94305, United States*

** Corresponding author email: beatriz.de.la.fuente.perez@vub.be*

‡ Equal contribution

TOC graphic

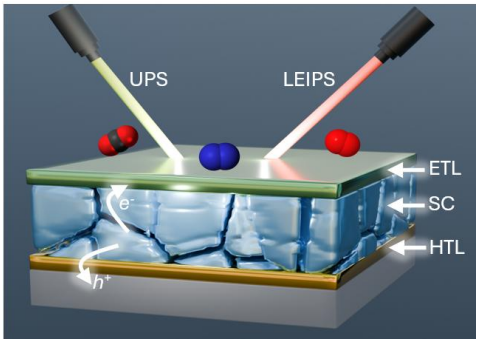

Schematic illustration of the device structure comprising a hole transport layer (HTL), semiconductor absorber, and electron transport layer (ETL). Ultraviolet photoelectron spectroscopy (UPS) and low-energy inverse photoelectron spectroscopy (LEIPS) are employed to probe the energy levels. Representative molecular targets (H_2, CO_2, and N_2) highlight potential photoelectrochemical applications for hydrogen production, CO_2 or N_2 reduction.

Abstract

Accurate determination of the conduction band minimum (CBM) is essential for designing efficient photoelectrochemical (PEC) systems, as it governs charge separation, transfer, and catalytic activity at interfaces. However, conventional techniques often lack the sensitivity or resolution needed to reliably measure absolute CBM positions. In this work, we directly determine the absolute energy positions of the valence band maximum (VBM) and CBM from key chalcogenide semiconductors (Cu_3BiS_3, $Cu(In,Ga)S_2$, Sb_2S_3, $Ag_2CuZnSnS_4$, and $Ag_2CuZnSn(S,Se)_4$) as well as the most significant hole and electron transport layers (HTL/ETL) for PEC applications using a combined approach of Ultraviolet Photoelectron Spectroscopy (UPS) and the less-explored Low-Energy Inverse Photoelectron Spectroscopy (LEIPS). These measurements revealed quantitative band-edge positions essential for understanding interfacial energetics and alignment with redox potential reactions. Our results provide a clear and robust framework for tailoring semiconductor interfaces with electrolytes or transport layers, thereby supporting targeted material screening and advancing the design of high-performance solar-to-X systems.

Introduction

Solar energy remains one of the most promising sustainable options for transitioning from fossil fuels to renewable energy technologies due to its abundance and scalability.[1-4] The development of earth-abundant and non-toxic semiconductors continues to be a central challenge. Chalcogenide-based materials, such as the extensively studied $CuInGaS_2$ (CIGS)[5-7], and Sb_2S_3[8-11], as well as newer compounds such as $AgCu_2ZnSnS_4$ (ACZTS)[12-14], and Cu_3BiS_3 (CBS)[15, 16] are a class of materials characterized by strong light absorption with high absorption coefficients (>10^4 cm^{-1}), a suitable bandgap (1.1-1.7 eV), tunable electronic properties, and high compatibility with solution or vacuum-based deposition methods, making them ideal for energy applications.[17] These materials have shown promise in photovoltaic and photoelectrochemical (PEC) applications, yet their performance remains highly variable and often difficult to predict across different device configurations.

In PEC applications, the semiconductor's performance is limited by low photocurrent densities and instability in an aqueous environment,[18, 19] which could be attributed to inadequate control over the quality of the thin film or its electronic properties.[20-22] A key determinant of functionality in PEC devices is the alignment of energy levels at the semiconductor interface, more specifically, the absolute position of the valence band maximum (VBM) and conduction band minimum (CBM) relative to the vacuum. The position of the bands governs charge transfer kinetics, redox compatibility, and interface energetics with electrolytes or transport layers.[21, 23, 24] However, for many emerging materials, direct and accurate experimental determination of electronic band levels remains challenging. Both experimental and theoretical data on the electronic band structure of this class of materials are currently limited.[8, 12] Band-edge positions are typically estimated using electrochemical techniques such as Mott Schottky[25, 26] or, more recently, cyclic voltammetry[27] as well as Kelvin probe force microscope[28] and theoretical calculations.[29-31] These approaches may suffer from environmental artifacts, contact effects, absorber instability due to long exposure in electrolyte media,[32] or assumptions about band alignment.[33] Additionally, they do not account for effects such as electron-electron interactions and band structure distortions that can affect the real electronic structure of the material.[34, 35] Therefore, understanding and optimizing band alignment and charge transport mechanisms are crucial for improving efficiency and long-term performance.

In this work, we report a systematic and direct approach for probing the electronic structure of emerging chalcogenide semiconductors using a contact-free, vacuum-referenced methodology.

By combining low-energy inverse photoelectron spectroscopy (LEIPS) and ultraviolet photoemission spectroscopy (UPS), we precisely determine the absolute energy positions of both CBM and VBM positions[36-40] under ultrahigh vacuum (Figure S2-S3-S4, and Table S1-S2). This approach eliminates reliance on inferred band alignments or bulk electronic assumptions and provides a broadly applicable framework for energy level mapping, particularly relevant for materials with strong excitonic effects such as 2D perovskites and conjugated organic ligands.[24] The measured band-edge positions were benchmarked against standard redox potentials to evaluate the thermodynamic driving forces for key reduction reactions. Additionally, we screened a set of transport layers (HTLs/ETLs) to identify those with optimal band alignment, facilitating efficient interfacial charge extraction and transport, and ultimately enhancing the performance potential of chalcogenide-based solar absorbers.

Materials and methods

Materials fabrication

All the substrates were ultrasonically cleaned with soaped water, deionized water (DI), acetone, and isopropanol for 15 min each.

Copper-bismuth-sulfide (Cu_3BiS_3, CBS) thin films were prepared via solution processing following the report from Huang et. al.[41] The fabrication involves the spin coating (Laurell, WS-650) of an ink solution on ITO substrate (Colorado Concept Coatings LLC). The substrates were subjected to a UV/Ozone treatment of 15 min to enhance the wettability. The ink solution is based on the mixture of bismuth chloride ($BiCl_3$, >99.99%), cuprous chloride (CuCl, 97%), dimethyl sulfoxide (DMSO, > 99%), and thiourea (Tu, >99.99%). To obtain the stoichiometric Cu_3BiS_3, Bi/Cu= 0.33 mole ratio was prepared. In one vial it was mixed CuCl (2M), DMSO (5mL), and thiourea (excess) to prepare ink-I; in another vial, it was mixed $BiCl_3$ (0.666 M), DMSO (5mL), and thiourea (excess) to prepare ink-II. Each ink solution was stirred for 1h. After that, ink-I and ink-II were mixed and stirred for 5h to obtain a yellowish clear stock solution ready for deposition. The precursor solution was subsequently deposited onto the ITO/glass substrate at 3000 rpm for 30 s and annealed at 300 °C.

$CuInGaS_2$ thin films were fabricated by sulfurizing CuInGa multi-stack films as described by Shukla et al.[6] Briefly, CuGa/In (CIG) was deposited on 500 nm of back contact Mo. In sequence, the CIG precursors were annealed in N_2 at 200ºC, followed by its sulfurization to obtain CIGS layers. The sulfurization was performed in an Annealsys system, which consists of a reaction of the CIG precursors with H_2S gas. First, the precursors were placed in the

Annealsys chamber and submitted to a stabilizing temperature at 150 ºC. Sulfurization occurred at 580 ºC at a ramping rate of 2.4 ºC/s. After 30 mins of annealing, the system is first cooled down to 150 ºC, and then cooled down naturally until room temperature is reached.

ACZTS(Se) thin films were fabricated according to the report by Zhou et. al.[42] Precursor inks were spin-coated onto a soda lime glass substrate coated with Mo. For that, 717.76 mg of Cu(I)Cl and 115.45 mg of Ag(I)Cl were dissolved in 5 ml of 2ME with 2100 mg of TU in one vial. In another vial with 5 ml of 2ME, 1040.6 mg of Zn(II)$(Ac)_2$ and Sn(IV)Cl_2 were dissolved. Both solutions were stirred at room temperature until fully dissolved, then mixed to form 10 ml of precursor ink. Spin-coating was performed 6 times to achieve the desired film thickness at 3000 rpm speed for 40 seconds, followed by solvent evaporation on a hot plate at 260 °C for 2 minutes after each deposition. In sequence, a sulfurization process using an Annealsys system was performed at 550 °C for 60 minutes and with a ramp rate of 0.7 °C/sec.

To synthesize small-bandgap Ag-doped $Cu_2ZnSn(S,Se)_4$ films, the same spin coating and annealing in the hot plate conditions was performed. However, a selenization process instead took place. For that, the precursor films were selenized in a graphite box with 100 g of Se-pellets, heated to 500 °C at 0.7 °C/sec, and annealed for 20 minutes.

The fabrication procedure of Sb_2S_3 was described in Dei Tos at al.[43] The fabrication happens in two steps: i. evaporation of Sb_2S_3, followed by ii. its sulfurization. Briefly, substrates were placed in an evaporation chamber with 150 mg of Sb_2S_3 powder (Sigma-Aldrich). The deposition process occurred at 530 °C for 30 seconds at a pressure of 10^{-5} mBar and cooled down to room temperature (RT). The sulfurization of the samples was done in a two-zone tube furnace containing two thermocouples, which allows adequate control over the temperature. On one side of the tube, the samples were placed, while the other zone was occupied by a quartz crucible containing 100 mg of sulfur powder (Sigma-Aldrich). The samples were annealed at 335 °C for 15 minutes using a ramping rate of 10 °C/min, while the sulfur powder was heated up to 200 °C. Once the process was finished, the samples were slowly cooled down to RT inside the tube furnace.

Characterization techniques

The SEM images are recorded with a Zeiss Gemini 450 FEG-SEM. The morphology of the samples is revealed through secondary electron images acquired at a low accelerating voltage (5 kV).

The crystallinity and phase formation on chalcogenide-based thin films were carried out by XRD with a Bruker D8 Advance equipped with a Lynxeye detector and operated with Cu-K_α X-ray (λ = 1.5418 Å) radiation.

Chemical and band structure analyses were conducted using a multi-technique X-ray photoelectron spectroscopy (XPS) system (VersaProbeIV, ULVAC-PHI, Inc.) equipped with UPS and LEIPS. Data processing was performed using MultiPak software (ULVAC-PHI, Inc). XPS spectra curve fitting and quantification were done with CasaXPS software (version 2.3.24PR1.0). The sensitivity factors used were taken from the MultiPak Software manual (v. 9). The line shape of the different components used in the fitting was a Gaussian - Lorentzian line shape (GL(30)). Calibration of the binding energy (BE) scale of every sample was done by associating the C-C/C-H component from the C1s high-resolution spectra to its respective BE at 284.8 eV.

XPS analyses were collected using an Al Kα anode and a main chamber pressure of ~5×10^{-7} Pa. The photoelectron analyzer is positioned at an angle of 45° with respect to the sample normal. A precise Z-height calibration was ensured before spectra collection to maximize the photoelectron signal. The selected pass energies were 224 eV and 55 eV, and the step sizes were 0.8 eV and 0.1 eV for the surveys and high-resolution scans, respectively. The electron and ion gun neutralizers were employed for all collections.

To obtain information on the VBM and ionization potential (IP), UPS was performed using a He I (21.22 eV) light source (wavelength of 58.4 nm). UPS spectra from each sample were collected in an unbiased condition, and again, the stage was biased to -10 V for the biased collection. The UPS system was calibrated using a silver (Ag) reference sample, following ISO standards,[44] to ensure accurate alignment of the energy scale. This procedure establishes the Fermi level and allows for precise determination of the secondary electron cut-off and VBM position, which are essential for calculating energy level parameters and constructing band diagrams. To obtain information on the CBM and electron affinity (EA), LEIPS spectra were acquired using low-energy electrons (< 5 eV). A quartz lens was used to gather the near-ultraviolet light that the sample surface released. A photomultiplier was then used to amplify the photon signals, which were sent through a band-pass filter. The selected bandpass filter energy (*bpf* energy) was 4.77 eV, which corresponds to a wavelength of 260 nm. The arriving photons are collected and filtered around that wavelength. The condition for selecting an appropriate filter is that *bpf* energy > EA of the studied semiconductor. The incident electron beam settings were 1 μA for the incident beam current and 40V for the acceleration voltage. LEIPS acquisition parameters were set to a step size of 0.04 V and a time per step of 2000 ms.

Compared to conventional IPES, LEIPS uses low-energy electrons to avoid sample damage. In a LEIPS experiment, a beam of low-energy electrons (E_k) hits the sample with less than 5 eV energy (low enough energy to avoid damaging the sample), creating a flow of electrons (negative current) into the sample. This flow produces a low-energy electron transmission (LEET) current spectrum.

Next, a bias is applied through the stage to slow down and then repel the incoming electrons. When the repelling voltage equals E_k, the electrons turn around, at zero kinetic energy. We define this as the inflection point of the LEET spectra (VI). The VI point also tells which applied voltage is needed to get electrons to the vacuum level. An illustration of the procedure used to determine VI from the derivative of the LEET current spectrum is provided in Figure S5 in SI.

LEIPS photons are detected with $h\nu$ = 4.77 eV, which is determined by the choice of the bandpass filter. Subtracting the difference between the onset of LEIPS (VL) and the LEET inflection point (VI) from the bandpass filter energy gives EA, as shown in Equation 1.

$$EA = h\nu - (VL - VI) \quad \text{(Eq. 1)}$$

When recording LEIPS and LEET spectra, minimal spectral shifting is desirable, as it generally indicates a stable surface potential during measurement. Shifts in the spectra typically reflect changes in the sample's effective potential, which may arise from surface charging or instrumental instabilities.

In LEET, it is common to observe spectra shifting toward more negative kinetic energies (i.e., from right to left in the energy axis). This behavior may result from sample charging or from equilibration processes between the sample and the LEIPS electron gun, which uses the sample as its final electrode. In some cases, these shifts stabilize over successive scans, especially after the first cycle, which often appears anomalous and is routinely discarded. However, not all samples exhibit convergence, particularly those with more insulating properties, which may continue to charge throughout the measurement.

Occasionally, we have observed the opposite trend, LEET spectra shifting toward less negative kinetic energy over time. The cause of this is unclear; it may be related to sample-specific effects or instrumentation drift, such as instability in the electron neutralizer (E-neut). Due to the complexity of these measurements and the limited data available, we refrain from drawing definitive conclusions about the mechanisms underlying spectral shifts.

To ensure the highest possible data quality, we discard the initial few scans (typically three) in both LEIPS and LEET measurements and only analyze spectra collected after reaching visual stability. After this equilibration period, the spectra remained stable within ±0.05 eV. The

overall measurement uncertainty, including instrument resolution, fitting error, and sample variation, was estimated at ±0.07 eV, based on repeated scans of the same samples. This consistency supports the use of three significant figures in reporting energy values.

All samples were mounted using a dedicated LEIPS sample holder provided by the manufacturer. This holder includes a molybdenum metallic shield with a 5 mm aperture and gold foil inserted between the shield and sample, ensuring good electrical grounding and helping minimize charging during both LEIPS and LEET measurements. Other recommended alternative methods to ensure proper electrical conductivity include applying a conductive back contact using silver paste and/or copper tape between the sample and the conductive shield. To ensure sample cleaning before UPS/LEIPS measurements, a Gas Cluster Ion Beam gun (GCIB) was used with a beam voltage of 10 kV, a target current of 30 nA, and a raster size of 4 mm × 4 mm for approximately 2 minutes on the sample surface. These settings produce equivalent cluster sizes of approximately 2000 Ar^+ ions. Although structural changes within the ~1-2 nm sampling depth of UPS/LEIPS cannot be entirely excluded, GCIB treatment was applied with minimal exposure and consistent parameters across all samples to reduce potential surface damage.[45] XPS measurements before and after treatment confirmed stable elemental composition (only surface carbon was removed), indicating negligible preferential sputtering. The respective spot sizes of XPS and UPS were 200 μm and ~3 mm. Additional details regarding the extraction of electronic parameters and the LEIPS shift correction for spectra tracing are provided below.

The VBM and CBM values can be extracted using a linear approximation with MultiPak's Edge Tool and finding the intercept with the X-axis, as shown schematically in Figure S3 (b). To draw this graph, the UPS unbiased values and the LEIPS values (with the LEIPS shift correction performed) are plotted together. From the unbiased UPS spectra, we obtain the highest occupied molecular orbital (HOMO) value ($HOMO_{UPS}$). From the biased UPS spectra (not shown), we obtain the secondary electron cut-off ($E0_{UPS}$) and the valence band maximum ($EVBM_{UPS}$). From the LEIPS spectrum, we obtain the conduction band minimum (ECBM). From the LEET, we obtain the LEET inflection point ($E0_{LEIPS}$). The UPS unbiased spectra are used to extract the E_F-VBM difference and then obtain the Fermi level E_F. With all those values, we extract E_{vac}, EA, IE, and BG, as described in the equations below.

$$Evac = HOMO_{UPS} - IP \quad \text{(Eq. 2)}$$

$$IP = hv_{UPS} - (E0_{UPS} - EVBM_{UPS}) \quad \text{(Eq. 3)}$$

$$EA = LEIPS_{bpf} - (ECBM - E0_{LEIPS}) \quad \text{(Eq. 4)}$$

$BG = IP - EA$ (Eq. 5)

LEIPS Shift Correction for Spectra Tracing

From the collected UPS and LEIPS spectra, the values of the important parameters are calculated using a linear extrapolation of the leading edge with the MultiPak software. From the UPS-biased measurement, we determine the value of the secondary electron cut-off and VBM and thus obtain the value of the IP. From the UPS unbiased measurement, we determine the value of the HOMO level. LEET and LEIPS collected signals give us the $E0_{LEIPS}$ and ECBM values, respectively, needed to determine the EA. To obtain all the energy with respect to the vacuum level, the LEIPS spectra are shifted based on Equation 6, in which the value of E_{vac} comes from the unbiased UPS spectrum. This procedure allows the depiction of all three spectra on the same energy scale.

$LEIPS_{shift} = E_{vac} - E0_{LEIPS} - bpf$ (Eq. 6)

Assumptions for NHE vs Vacuum

To relate the vacuum-based measurements to an electrochemical energy scale, two additional key aspects must be considered: the energetics of the absorber surface can change in the presence of an electrolyte, and the effects of changing pH. We followed a similar approach from Carter[21] on chalcopyrite materials. The assumptions made are the following:

Regarding the difference in band bending between absorber/vacuum vs absorber/electrolyte interfaces due to the formation of an electrical double layer (EDL), the additional band bending in the case of chalcopyrite materials is expected to be relatively small. This assumption is also adopted in the case of chalcogenides. Concerning the difference in pH, we also assume that since the desired pH value for a given chalcogenide PEC cell is a priori not known, all energy diagrams are represented under the assumption of pH = 0 for connecting the NHE scale and the vacuum level scale.

Under these assumptions[21], the band edge energies at the surface determined under vacuum conditions, shown in Figure 3, can be visualized on an electrochemical energy scale relevant to PEC devices [i.e., relative to the normal hydrogen electrode (NHE)] with the help of the work function determined in the same experiments.

$-E(NHE) - 4.44 \pm 0.02\ eV = Evac$ (Eq. 7)

Results and discussion

Photocatalysts Characterization

A comprehensive characterization of the synthesized materials was conducted to ensure their structural integrity and phase purity before investigating their electronic properties. X-ray diffraction (XRD) analysis was performed to confirm phase composition and detect any secondary phases. Figure S6 shows the X-ray diffractogram of CBS, CIGS, Sb_2S_3, ACZTS, and ACZTSSe. CBS data match well with the orthorhombic wittichenite reference positions (space group 19, $P2_12_12_1$, JCPDS No. 01-071-2115), in agreement with other reports.[41, 46] The CIGS diffractogram revealed a highly crystalline chalcopyrite phase well indexed to the tetragonal structure (space group $\bar{I}42d$), which is in agreement with other reports.[47-49] Extra peaks are observed at around 13° and 27° degrees, attributed to the $NaInS_2$ phase, which originated from diffusion from the soda lime glass substrate. The Sb_2S_3 diffractogram shows pure phase formation without secondary phases. The peaks match well with the orthorhombic structure (space group Pbnm (JCPDS No. 42-1393)), as observed in other reports.[50, 51] The presence of both the hk1 and hk0 planes revealed a randomly oriented grain structure with various facets. The ACZTS diffractogram showed that the major phase of the thin film is the desired kesterite (CZTS) phase (JCPDs No. 26-0575), and a minor peak of Ag_2ZnSnS_4 around 44.1° degrees, as reported elsewhere.[52] The same structure is observed for ACZTSSe, with the addition of a shift from 28.3° to 27.2° degrees, which confirms the successful substitution of selenium in the desired phase, as observed in other reports.[53]

The morphology of the top surface and cross-section of CBS, CIGS, Sb_2S_3, ACZTS, and ACZTSSe semiconductors was examined via scanning electron microscopy (SEM) and depicted in Figure 1. CBS exhibited a compact film with an interconnected cuboid morphology, characterized by large grains across its surface. CIGS appeared polycrystalline with a dense distribution of large and small grains over the surface. For Sb_2S_3, SEM imaging showed planar, packed, and large grains over the surface. The ACZTS morphology revealed a bimodal grain size distribution characterized by a mixture of small and large compact grains. By contrast, ACZTSSe exhibits a more uniform grain structure that is predominantly composed of larger grains. All investigated materials exhibit a continuous grain, with no observable vertical voids or pinholes extending from the top surface to the substrate. This uninterrupted structure is crucial for PEC applications, where structural discontinuities can provide direct pathways for electrolyte penetration. This could result in undesired contact between the electrolyte and the underlying conductive substrate, leading to shunting[54] and device degradation.[55] The absence of through-film voids thus indicates a structurally robust thin film architecture.

To further validate the phase identification of the chalcogenide semiconductors, X-ray photoelectron spectroscopy (XPS) was performed to analyze surface chemistry and oxidation states. A gentle GCIB cleaning process minimized surface carbon contamination before analysis (< 4%). The XPS survey spectra for CBS, CIGS, Sb_2S_3, ACZTS, and ACZTSSe before and after GCIB cleaning are shown in Figure S8. The binding energies of various elements in CBS, CIGS, Sb_2S_3, ACZTS, and ACZTSSe (Figures S9 to S13) confirm the presence of expected oxidation states for Cu^{+}, Bi^{3+}, In^{3+}, Ga^{3+}, Sb^{3+}, Ag^{+}, Sn^{2+}, S^{2-}, and Se^{2+}, validating the synthesis and its consistency with the intended design.[8, 10, 12-14, 16, 56-58] The full discussion on the core levels and interpretation is provided in the SI. These results confirm that thin films are suitable for electronic band structure measurements.

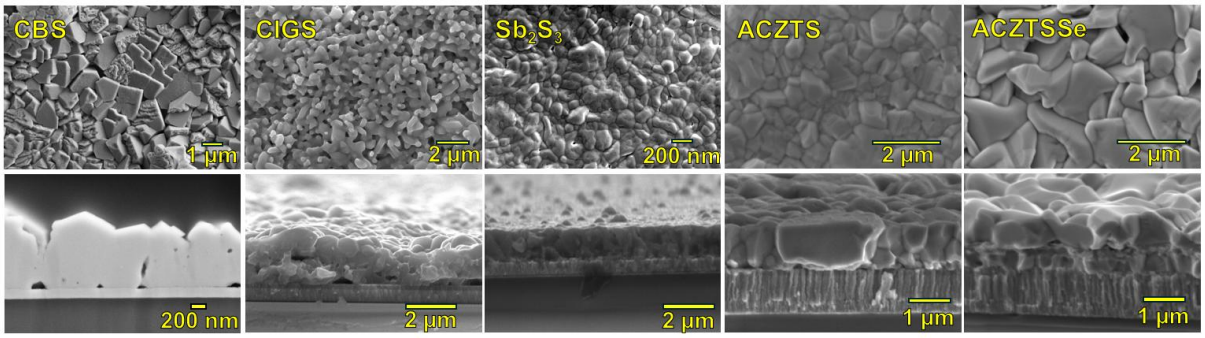

Figure 1. Top row: surface scanning electron microscopy (SEM) images of CBS, CIGS, Sb_2S_3, ACZTS, and ACZTSSe chalcogenide semiconductors. Bottom row: Corresponding XSEM images aligned vertically below each SEM image to facilitate comparison. Different magnifications were used to better capture the characteristic features of each material.

Electronic structure of standalone chalcogenide absorbers

To accurately determine the electronic structure of the chalcogenide absorber, we performed UPS and LEIPS measurements. These complementary techniques allow direct probing of the VBM and CBM positions, respectively, with respect to the vacuum level. Figure 2 shows the UPS/LEIPS spectra for all the chalcogenide absorbers studied. Via linear extrapolation of the leading edges of the UPS and LEIPS spectra, we extract electron affinity (EA) and ionization potential (IP), respectively, as depicted in Figure S3. These spectra provide information about the IP, EA relative to the vacuum level. These key parameters are critical to understanding how energy levels will align at interfaces. The IP represents the energy required to remove an electron from the valence band, which can provide insights into the material's stability and hole

transport characteristics. By contrast, EA defines the ability of a material to accept electrons, which can affect its conduction band properties and electron transport efficiency. The difference between vacuum levels is determined via the inflection point of the LEET, and CBM/VBM values are used to determine the IP and EA, respectively. All extracted electronic parameters are reported in Table S2. These values are in accordance with previously reported density functional theory (DFT) analysis.[7, 10, 16, 59] LEIPS analysis revealed a CBM of 3.93, 4.52, 3.78, 3.82, and 4.01 eV *vs*. vacuum level, yielding fundamental electronic bandgaps (E_g) of 1.07, 1.68, 1.83, 1.60, and 1.32 eV for CBS, CIGS, Sb_2S_3, ACZTS, and ACZTSSe, respectively. These values are in good agreement with the reported optical bandgap values estimated via Tauc plot analysis or photoluminescence, confirming the reliability of our spectroscopic determination. Additionally, the position of the Fermi level (E_F) helps in understanding whether the semiconductor behaves as n-type (E_F lies close to the CBM) or p-type (E_F lies close to the VBM). The conductivity type influences how these materials interact at interfaces, which is crucial for semiconductor devices. Via the UPS unbiased spectra, we extract the E_F position for each absorber (demarcated and shown in Figure 3). E_F is 0.37, 0.59, 0.56, and 0.44 eV above the VBM for CBS, CIGS, ACZTS, and ACZTSSe, suggesting that these absorbers exhibit p-type character, meaning the majority of carriers are holes in the valence band. One of the reasons for the observed p-type behavior could be the presence of native defects such as metal vacancies (i.e., copper vacancies).[60, 61] These vacancies act as acceptor states that facilitate hole conduction.[62] In contrast, Sb_2S_3 exhibits E_F located within the bandgap, indicating its intrinsic nature rather than a strong n-type character (majority carriers are electrons). [9, 63] Due to its moderate bandgap and favorable band edge positions, Sb_2S_3 can thermodynamically support both reduction and oxidation half-reactions, making it suitable for photoelectrochemical applications. Additionally, intrinsic defects in the Sb_2S_3 crystal structure, such as vacancies or antisite defects, can introduce mid-gap states.[64-66] These states may also contribute to Fermi level pinning, especially when the density of states associated with defects is high.[67] These direct absolute energy levels establish a foundational understanding of the material's potential to participate in charge separation and transport processes, while overcoming the limitations of relying on indirect estimations or theoretical assumptions.

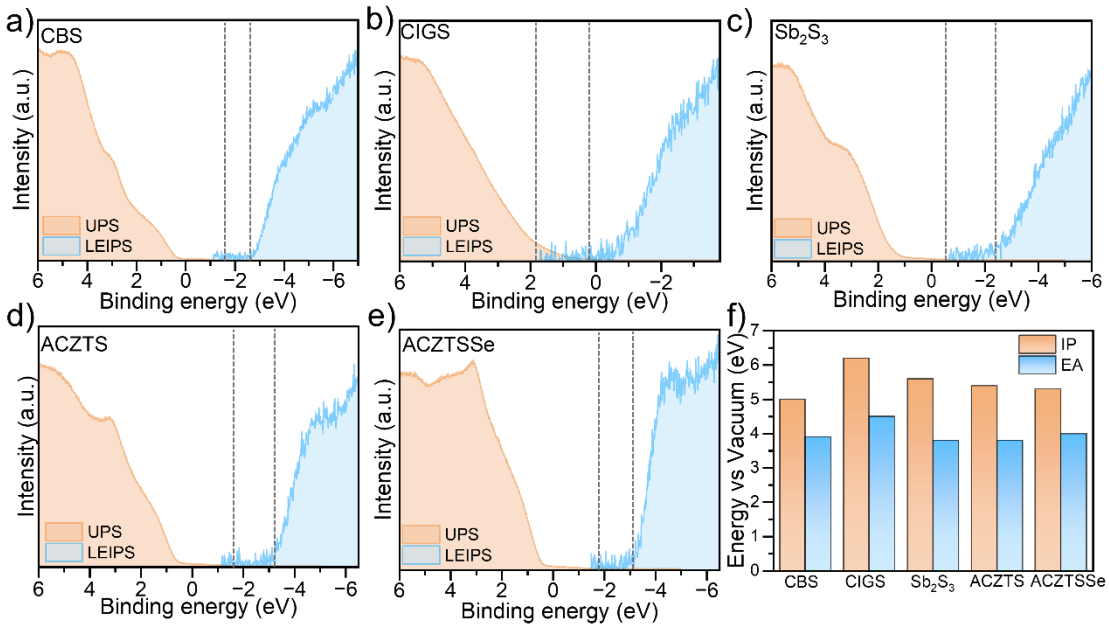

Figure 2. The band structure characterization by combining UPS and LEIPS spectra for a) CBS, b) CIGS, c) Sb_2S_3, d) ACZTS, e) ACZTSSe photoelectrodes, and f) ionization potential (IP) and electron affinity (EA) extracted values from UPS/LEIPS. The magnified graphs in Figure S4 highlight the initial, previously non-visible bump in the unbiased UPS spectra, which is essential for accurately determining the HOMO level.

Thermodynamic viability of PEC reactions

To evaluate the suitability of the studied absorbers for efficient PEC applications, their band edges must appropriately straddle the redox potentials of the target reactions.[68, 69] Misalignments can result in inefficient charge transfer, slow reaction kinetics, or enhanced charge recombination, all of which limit photocatalytic performance.[10, 16, 59] In this context, we analyze the band alignment of the different photo absorbers with respect to key PEC reactions. The absolute vacuum-referenced energy levels were converted to the normal hydrogen electrode (NHE) scale using the relation described in Eq. 7 in SI. Figure 3 illustrates the extracted band diagrams alongside the redox potentials of the most commonly studied reactions: the carbon dioxide reduction reaction (CO_2RR), the hydrogen evolution reaction (HER), the oxygen evolution reaction (OER), and the nitrogen reduction reaction (NRR). Figure S7 depicts the ideal band edge positions relative to the redox potential necessary for the respective reactions to occur. All photo absorbers investigated exhibit VBM at or above 0 V vs. NHE and CBM at more negative potentials. These alignments satisfy the thermodynamic criteria for HER, enabling photogenerated holes to drive oxidation and electrons to reduce

protons to molecular hydrogen.[70] In the case of PEC CO_2RR, CBS, Sb_2S_3, ACZTS, and ACZTSSe exhibited VBM near or above 0 V vs NHE and CBM more negative than –0.11 V vs. NHE, satisfying the thermodynamic criteria for CO_2 reduction to CO. However, their CBM lies substantially below the CO_2/CO redox potential, resulting in slow electron transfer kinetics due to excessive overpotential. [21, 70] In contrast, CIGS exhibits a CBM (-0.06 vs NHE) that is well-aligned with the redox potential of the CO_2-to-CO reaction, promoting more efficient electron transfer and potentially improving the reaction kinetics and selectivity. This alignment underscores CIGS's suitability for PEC CO_2RR applications compared to the other absorbers studied. For NRR, ACZTS, and ACZTSSe VB are positioned above the NHE potential for NRR (at 0.00 V vs NHE), and CBMs are at -0.64 and -0.44 V vs. NHE, respectively, which means that they are at a more negative potential than the reduction potential of N_2 (around 0.50 V vs. NHE for $N_2 \rightarrow NH_3$ at neutral pH). This is because the CBM needs to be sufficiently negative to facilitate the electron transfer required to break the strong N≡N bond.[71] For OER, Sb_2S_3, due to its intrinsic characteristics, is the only suited candidate to drive this reaction and its CBM is at -0.64 V vs NHE, below the water reduction potential (0 V vs NHE). Its VBM (1.16 V vs. NHE) is, from all the absorbers, the closest (but also slightly below) to the OER (1.23 V vs. NHE) in acidic conditions (i.e., pH 0), indicating favorable energetics for water oxidation.[70, 72]

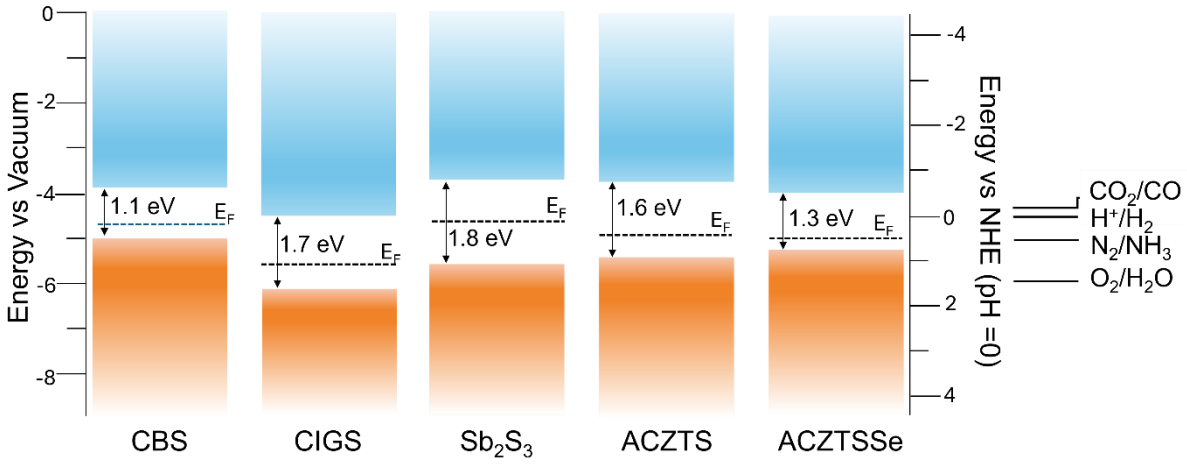

Figure 3. a) Schematic energy band diagram relative to the vacuum level and normal hydrogen electrode (NHE) for CBS, CIGS, Sb_2S_3, ACZTS, and ACZTSSe photo absorbers. The band gap and E_F values were extracted from UPS and LEIPS spectra referenced to the vacuum level.

Interfacial energy level alignment: HTL/ETL candidates screening

While absorbers may possess favorable electronic properties, they require significant interfacial engineering to achieve high PEC efficiency. To facilitate efficient charge extraction and suppress recombination losses, appropriate band alignment between the photoabsorber and charge transport layers (hole transport layer (HTL) or electron transport layer (ETL) is essential. [73-77] We measured the CBM and VBM positions, via UPS/LEIPS, of the most commonly used HTLs and ETLs materials in devices for favorable energetic alignment with the absorbers. Here, we investigated NiO, TiO_2, ZnO, CdS, and CuI[78], and SnO_2[29] were taken from the literature. An ideal HTL should have a VBM near the absorber's VBM to enable efficient hole transfer with minimal energetic barrier. Similarly, an ideal ETL should have a CBM slightly below that of the absorber to ensure efficient electron transfer and suppress recombination in devices. Figure 4 depicts the resulting energy level diagram, with all the values referenced to the vacuum level, for the HTL, absorbers, and ETL materials. The alignment analysis allows for visual identification of potential barriers or offsets at the transport interfaces. For HTL screening, NiO exhibited the closest alignment with the VBM of CBS with an offset of 0.1 eV. Although NiO exhibits close alignment with the valence band maximum (VBM) of CBS, efficient charge transport cannot be determined solely from the conduction and valence band positions. In practice, Fermi level alignment and interfacial effects, such as defect states and possible Fermi level pinning, play a critical role in governing charge transfer efficiency.[79] In contrast, it exhibits a significant mismatch (>0.4 eV) with the other semiconductors tested, indicating a less favorable interfacial contact for hole transport. CuI provides suitable offsets within or close to the ideal 0.1-0.3 eV range for Sb_2S_3, ACZTS, and ACZTSSe. While the alignment with CIGS is better than that of NiO, a 0.4 eV offset remains, which may still hinder efficient hole extraction.

The ETL screening reveals that CdS provides nearly ideal alignment with all the semiconductors, featuring negligible electron injection barriers (0.1-0.3 eV). A similar trend is observed for SnO_2 and ZnO: in most cases, there is a significant valence band offset with the absorber, except for CIGS, which has a much deeper VBM relative to the ETLs. In the cases of Sb_2S_3 and ACZTSSe, the CBM of SnO_2 is nearly aligned with that of the absorber, an observation also seen for ZnO and CBS. Such near-flat band alignment may result in minimal driving force for electron transfer, potentially limiting charge extraction efficiency. TiO_2, despite being commonly employed in PEC systems, exhibits a relatively large conduction band offset with the semiconductors, which may hinder charge extraction efficiency or lead to interface recombination. This can be attributed to the fact that, in many PEC architectures, TiO_2

serves primarily as a protective or passivation layer rather than as an efficient ETL.[80] In these cases, TiO_2's role is to provide chemical stability against corrosion and suppress surface recombination, rather than to facilitate direct charge transport. As a result, TiO_2 is often combined with additional interlayers (e.g., SnO_2)[81, 82] to bridge the energetic mismatch and enhance charge collection efficiency. While the alignment of HTL and ETL with the absorber defines the charge injection and extraction barriers, the actual energy landscape at the interface, influencing band bending, charge carrier injection barriers, and recombination processes, is ultimately governed by the Fermi level position at equilibrium. The measured Fermi levels of all hole transport layers (HTL) and electron transport layers (ETL) are summarized in Figure 4 and Table S3. These observations underscore the importance of LEIPS/UPS and rational ETL/HTL selection tailored to each absorber's band structure in rapidly screening candidates for PEC applications. Energy levels are aligned relative to the vacuum level for comparison purposes only. In actual interfaces, however, Fermi level equilibration and interface-specific phenomena (such as dipole formation and band bending) govern the true energy level alignment.[39, 83] Unlike simulation-based approaches that rely on idealized input parameters, LEIPS/UPS offers direct, accurate experimental insight into energy levels and interfacial alignment. Incorporating such layers could significantly boost overall PEC efficiency through improved interfacial energetics and carrier selectivity.

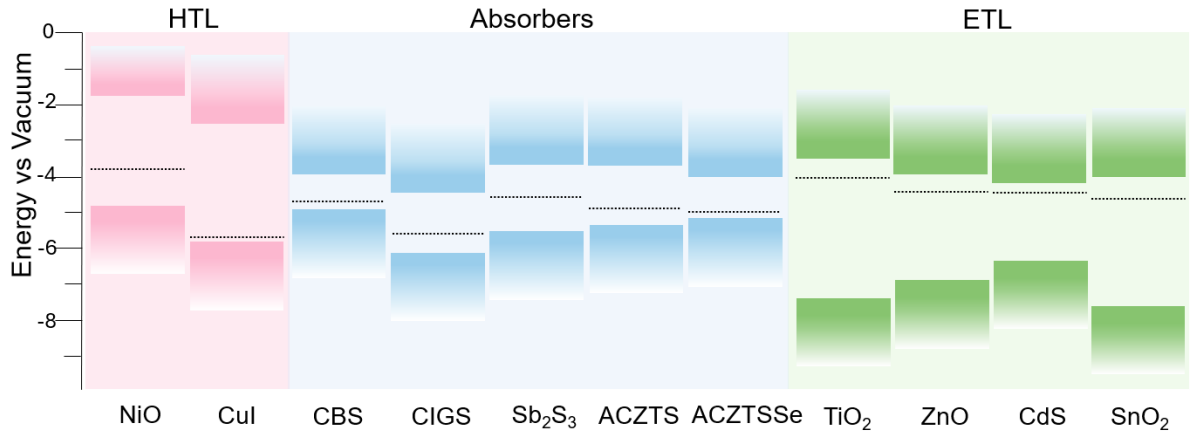

Figure 4. Energy level diagram comparing CBM/VBM from LEIPS/UPS for CBS, CIGS, Sb_2S_3, ACZTS, and ACZTSSe semiconductors, HTL level from NiO and CuI; ETL levels from TiO_2, ZnO, CdS, and SnO_2. Literature values of CBM, VBM, and E_g are taken for CuI[78] and SnO_2[84]. The dashed line corresponds to the Fermi level position.

Conclusions

We present a direct experimental determination of absolute valence and conduction band edges for key chalcogenide absorbers and transport layers using UPS and LEIPS. Our results reveal that all studied absorbers meet the thermodynamic criteria for hydrogen evolution, while CIGS uniquely aligns well for efficient CO_2 reduction. Sb_2S_3 stands out for oxygen evolution, and ACZTS/ACZTSSe show promise for nitrogen reduction. Proper interfacial energy alignment is essential for efficient charge transport. NiO and CuI serve as effective hole transport layers for selected absorbers, whereas CdS proves to be the most broadly compatible electron transport layer. TiO_2, despite common use, shows a significant energetic mismatch, underscoring the need for careful interface engineering or additional interlayers. This experimental band mapping offers a powerful tool for rational materials selection, enabling optimized charge transfer and reduced recombination in PEC devices. These findings establish a clear pathway to tailor absorber/transport layer combinations, accelerating the design of efficient, stable photoelectrochemical solar fuel systems.

Corresponding Author

Research group Sustainable Materials Engineering (SUME), Lab of Electrochemical and Surface Engineering (SURF), Vrije Universiteit Brussel, Pleinlaan 2, Brussels 1050, Belgium**;** orcid.org/0000-0001-9045-3481; Email: beatriz.de.la.fuente.perez@vub.be

Supporting Information

Schematic PEC mechanisms; publication trends of UPS/IPES/LEIPS; UPS and LEIPS data analysis; band structure magnification; XRD patterns of CBS, CIGS, Sb_2S_3, ACZTS, ACZTSSe; ideal band edge alignment diagram; XPS survey and high-resolution spectra before/after GCIB cleaning; comparison of IPES and LEIPS techniques; extracted electronic parameters; detailed XPS peak assignments.

Acknowledgments

B.D.‡ and D.R.S‡ equally contributed to this work. Part of this work was performed at the Stanford Nano Shared Facilities (SNSF) RRID:SCR_023230, supported by the National Science Foundation under award ECCS-2026822. This work was supported by a grant from the Fonds voor Wetenschappelijk Onderzoek - Vlaanderen (FWO) for B.D. visiting doctoral fellowship (No. V441024N). The authors acknowledge Catalisti VLAIO (Vlaanderen Agentschap Innoveren & Ondernemen) for their funding through the Moonshot SYN-CAT project (HBC.2020.2614). DRS and IDT acknowledge funds from the Fonds voor

Wetenschappelijk Onderzoek - Vlaanderen (FWO) for the Ph.D. fellowship (No. 11PJZ24N and No. 11PNM24N, respectively). SS acknowledges funding from the European Union's Horizon Europe program under the Marie Skłodowska-Curie Grant Agreement No. 101067667. The authors thank Gautam Virenutan for providing ACZTS(Se) samples.

Conflict of Interest

The authors declare no conflict of interest.

References

1. Nijsse, F. J. M. M.; Mercure, J.-F.; Ameli, N.; Larosa, F.; Kothari, S.; Rickman, J.; Vercoulen, P.; Pollitt, H., The momentum of the solar energy transition. *Nature Communications* **2023,** *14* (1), 6542.
2. Kraan, O.; Kramer, G. J.; Haigh, M.; Laurens, C., An Energy Transition That Relies Only on Technology Leads to a Bet on Solar Fuels. *Joule* **2019,** *3* (10), 2286-2290.
3. Palmer, G., Renewables rise above fossil fuels. *Nature Energy* **2019,** *4* (7), 538-539.
4. Gray, H. B., Powering the planet with solar fuel. *Nature Chemistry* **2009,** *1* (1), 7-7.
5. Guerrero, J.; Bajard, E.; Schneider, N.; Dumoulin, F.; Lincot, D.; Isci, U.; Robert, M.; Naghavi, N., Multifunctional Photovoltaic Window Layers for Solar-Driven Catalytic Conversion of CO2: The Case of CIGS Solar Cells. *ACS Energy Letters* **2023,** *8* (8), 3488-3493.
6. Prabhakar, R. R.; Shukla, S.; Li, H.; Kim, R. S.; Chen, W.; Beaudelot, J.; D'Haen, J.; Santos, D. R.; Vereecken, P. M.; Rignanese, G.-M., et al., Origin of photoelectrochemical CO2 reduction on bare Cu(In,Ga)S2 (CIGS) thin films in aqueous media without co-catalysts. *EES Catalysis* **2025,** *3* (2), 327-336.
7. Shukla, S.; Sood, M.; Adeleye, D.; Peedle, S.; Kusch, G.; Dahliah, D.; Melchiorre, M.; Rignanese, G.-M.; Hautier, G.; Oliver, R., et al., Over 15% efficient wide-band-gap Cu(In,Ga)S2 solar cell: Suppressing bulk and interface recombination through composition engineering. *Joule* **2021,** *5* (7), 1816-1831.
8. Cui, Z.; Bu, K.; Zhuang, Y.; Donnelly, M.-E.; Zhang, D.; Dalladay-Simpson, P.; Howie, R. T.; Zhang, J.; Lü, X.; Hu, Q., Phase transition mechanism and bandgap engineering of Sb2S3 at gigapascal pressures. *Communications Chemistry* **2021,** *4* (1), 125.
9. Kondrotas, R.; Chen, C.; Tang, J., Sb2S3 Solar Cells. *Joule* **2018,** *2* (5), 857-878.
10. Wang, L.; Lian, W.; Liu, B.; Lv, H.; Zhang, Y.; Wu, X.; Wang, T.; Gong, J.; Chen, T.; Xu, H., A Transparent, High-Performance, and Stable Sb(2) S(3) Photoanode Enabled by Heterojunction Engineering with Conjugated Polycarbazole Frameworks for Unbiased Photoelectrochemical Overall Water Splitting Devices. *Adv Mater* **2022,** *34* (29), e2200723.
11. Wang, X.; Ganose, A. M.; Kavanagh, S. R.; Walsh, A., Band versus Polaron: Charge Transport in Antimony Chalcogenides. *ACS Energy Letters* **2022,** *7* (9), 2954-2960.
12. Gansukh, M.; Li, Z.; Rodriguez, M. E.; Engberg, S.; Martinho, F. M. A.; Mariño, S. L.; Stamate, E.; Schou, J.; Hansen, O.; Canulescu, S., Energy band alignment at the heterointerface between CdS and Ag-alloyed CZTS. *Scientific Reports* **2020,** *10* (1), 18388.
13. Patil, S. J.; Lokhande, V. C.; Lee, D.-W.; Lokhande, C. D., Electrochemical impedance analysis of spray deposited CZTS thin film: Effect of Se introduction. *Optical Materials* **2016,** *58*, 418-425.
14. Suryawanshi, M. P.; Ghorpade, U. V.; Suryawanshi, U. P.; He, M.; Kim, J.; Gang, M. G.; Patil, P. S.; Moholkar, A. V.; Yun, J. H.; Kim, J. H., Aqueous-Solution-Processed Cu(2)ZnSn(S,Se)(4) Thin-Film Solar Cells via an Improved Successive Ion-Layer-Adsorption-Reaction Sequence. *ACS Omega* **2017,** *2* (12), 9211-9220.
15. Santos, D. R.; Shukla, S.; Vermang, B., Prospects of copper–bismuth chalcogenide absorbers for photovoltaics and photoelectrocatalysis. *Journal of Materials Chemistry A* **2023,** *11* (41), 22087-22104.
16. Whittles, T. J.; Veal, T. D.; Savory, C. N.; Yates, P. J.; Murgatroyd, P. A. E.; Gibbon, J. T.; Birkett, M.; Potter, R. J.; Major, J. D.; Durose, K., et al., Band Alignments, Band Gap, Core Levels, and Valence Band States in Cu(3)BiS(3) for Photovoltaics. *ACS Appl Mater Interfaces* **2019,** *11* (30), 27033-27047.
17. Woods-Robinson, R.; Han, Y.; Zhang, H.; Ablekim, T.; Khan, I.; Persson, K. A.; Zakutayev, A., Wide Band Gap Chalcogenide Semiconductors. *Chemical Reviews* **2020,** *120* (9), 4007-4055.
18. Colombara, D.; Elanzeery, H.; Nicoara, N.; Sharma, D.; Claro, M.; Schwarz, T.; Koprek, A.; Wolter, M. H.; Melchiorre, M.; Sood, M., et al., Chemical instability at chalcogenide surfaces impacts chalcopyrite devices well beyond the surface. *Nature Communications* **2020,** *11* (1), 3634.

19. Liu, D.; Kuang, Y., Particle-Based Photoelectrodes for PEC Water Splitting: Concepts and Perspectives. *Advanced Materials* **2024,** *36* (37), 2311692.
20. Morkel, M.; Weinhardt, L.; Lohmüller, B.; Heske, C.; Umbach, E.; Riedl, W.; Zweigart, S.; Karg, F., Flat conduction-band alignment at the CdS/CuInSe2 thin-film solar-cell heterojunction. *Applied Physics Letters* **2001,** *79* (27), 4482-4484.
21. Carter, J. C.; Hauschild, D.; Weinhardt, L.; Horsley, K.; Hariskos, D.; Gaillard, N.; Heske, C., Electronic Structure of Chalcopyrite Surfaces for Photoelectrochemical Hydrogen Production. *The Journal of Physical Chemistry C* **2023,** *127* (17), 8235-8246.
22. Weinhardt, L.; Blum, M.; Bär, M.; Heske, C.; Cole, B.; Marsen, B.; Miller, E. L., Electronic Surface Level Positions of WO3 Thin Films for Photoelectrochemical Hydrogen Production. *The Journal of Physical Chemistry C* **2008,** *112* (8), 3078-3082.
23. DuBose, J. T.; Kamat, P. V., Efficacy of Perovskite Photocatalysis: Challenges to Overcome. *ACS Energy Letters* **2022,** *7* (6), 1994-2011.
24. Lin, C.; Tang, Y.; Xu, W.; Kumar, P.; Dou, L., Charge Transfer in 2D Halide Perovskites and 2D/3D Heterostructures. *ACS Energy Letters* **2024,** *9* (8), 3877-3886.
25. Gelderman, K.; Lee, L.; Donne, S. W., Flat-Band Potential of a Semiconductor: Using the Mott–Schottky Equation. *Journal of Chemical Education* **2007,** *84* (4), 685.
26. Hankin, A.; Bedoya-Lora, F. E.; Alexander, J. C.; Regoutz, A.; Kelsall, G. H., Flat band potential determination: avoiding the pitfalls. *Journal of Materials Chemistry A* **2019,** *7* (45), 26162-26176.
27. Khurana, D. A.; Plankensteiner, N.; Vermang, B.; Vereecken, P. M., Reversible Redox Probes to Determine Band-Edge Locations and Dopant Concentrations of Nano-TiO2 Thin-Films: Settling the Mott-Schottky Conundrum. *Angewandte Chemie International Edition* **2025,** *64* (4), e202415857.
28. Markeev, P. A.; Najafidehaghani, E.; Gan, Z.; Sotthewes, K.; George, A.; Turchanin, A.; de Jong, M. P., Energy-Level Alignment at Interfaces between Transition-Metal Dichalcogenide Monolayers and Metal Electrodes Studied with Kelvin Probe Force Microscopy. *The Journal of Physical Chemistry C* **2021,** *125* (24), 13551-13559.
29. Hossain, M. K.; Toki, G. F. I.; Kuddus, A.; Rubel, M. H. K.; Hossain, M. M.; Bencherif, H.; Rahman, M. F.; Islam, M. R.; Mushtaq, M., An extensive study on multiple ETL and HTL layers to design and simulation of high-performance lead-free CsSnCl3-based perovskite solar cells. *Scientific Reports* **2023,** *13* (1), 2521.
30. Melitz, W.; Shen, J.; Lee, S.; Lee, J. S.; Kummel, A. C.; Droopad, R.; Yu, E. T., Scanning tunneling spectroscopy and Kelvin probe force microscopy investigation of Fermi energy level pinning mechanism on InAs and InGaAs clean surfaces. *Journal of Applied Physics* **2010,** *108* (2).
31. Iranzo-Marin, F.; Debiemme-Chouvy, C.; Herlem, M.; Sculfort, J.-L.; Etcheberry, A., Electrochemical techniques for the elucidation of the interface structure of the n-InP/aqueous electrolyte junction. *Journal of Electroanalytical Chemistry* **1994,** *365* (1-2), 283-287.
32. Min, S.; Jeon, M.; Cho, J.; Bang, J. H.; Kamat, P. V., Spectroelectrochemical insights into the intrinsic nature of lead halide perovskites. *Nano Convergence* **2024,** *11* (1), 49.
33. Shiel, H.; Hutter, O. S.; Phillips, L. J.; Swallow, J. E. N.; Jones, L. A. H.; Featherstone, T. J.; Smiles, M. J.; Thakur, P. K.; Lee, T.-L.; Dhanak, V. R., et al., Natural Band Alignments and Band Offsets of Sb2Se3 Solar Cells. *ACS Applied Energy Materials* **2020,** *3* (12), 11617-11626.
34. Sugie, A.; Nakano, K.; Tajima, K.; Osaka, I.; Yoshida, H., Dependence of Exciton Binding Energy on Bandgap of Organic Semiconductors. *J Phys Chem Lett* **2023,** *14* (50), 11412-11420.
35. Hill, I. G.; Kahn, A.; Soos, Z. G.; Pascal, J. R. A., Charge-separation energy in films of π-conjugated organic molecules. *Chemical Physics Letters* **2000,** *327* (3), 181-188.
36. Iida, S.-i.; Terashima, M.; Mamiya, K.; Kimoto, T.; Sasaki, S., Improving the Stability of Li Metal Anode/Solid Electrolyte Interfaces via an Li3PO4 Intermediate Layer: An Investigation of Surface Chemistry and Electronic Band Structure. *Journal of The Electrochemical Society* **2023,** *170* (9), 090503.

37. Terashima, M.; Mamiya, K.; Kimoto, T.; Sasaki, S.; Iida, S.-i., Selection of Surface Coating Materials for Ni-Rich NCM in All-Solid-State Batteries through Electronic Band Structure Analysis Using UPS/LEIPS. *The Journal of Physical Chemistry C* **2024,** *128* (22), 9393-9397.
38. Terashima, M.; Miyayama, T.; Shirao, T.; Mo, H. W.; Hatae, Y.; Fujimoto, H.; Watanabe, K., The electronic band structure analysis of OLED device by means of in situ LEIPS and UPS combined with GCIB. *Surface and Interface Analysis* **2020,** *52* (12), 948-952.
39. Klein, A., Transparent Conducting Oxides: Electronic Structure–Property Relationship from Photoelectron Spectroscopy with in situ Sample Preparation. *Journal of the American Ceramic Society* **2013,** *96* (2), 331-345.
40. Hou, H.; Wang, W.; Li, T.; Zhang, Z.; Miao, X.; Cai, G.; Lu, X.; Yi, Y.; Lin, Y., Efficient Infrared-Detecting Organic Semiconductors Featuring a Tetraheterocyclic Core with Reduced Ionization Potential. *Angewandte Chemie International Edition* **2025,** *64* (16), e202425420.
41. Huang, D.; Li, L.; Wang, K.; Li, Y.; Feng, K.; Jiang, F., Wittichenite semiconductor of Cu3BiS3 films for efficient hydrogen evolution from solar driven photoelectrochemical water splitting. *Nature Communications* **2021,** *12* (1), 3795.
42. Zhou, J.; Xu, X.; Wu, H.; Wang, J.; Lou, L.; Yin, K.; Gong, Y.; Shi, J.; Luo, Y.; Li, D., et al., Control of the phase evolution of kesterite by tuning of the selenium partial pressure for solar cells with 13.8% certified efficiency. *Nature Energy* **2023,** *8* (5), 526-535.
43. Shukla, S.; Tos, I. D.; Simbula, A.; Guerrero, J.; Dong, T.; Subramaniam, S.; Fuente, B. d. l.; Jose, V. K.; Aernouts, T.; Naghavi, N., et al., Elucidating Carrier Dynamics and Interface Engineering in Sb2S3: Towards Efficient Photoanode for Water Oxidation. *ChemSusChem n/a* (n/a), e202402764.
44. Pinder, J. W.; Major, G. H.; Baer, D. R.; Terry, J.; Whitten, J. E.; Čechal, J.; Crossman, J. D.; Lizarbe, A. J.; Jafari, S.; Easton, C. D., Avoiding common errors in X-ray photoelectron spectroscopy data collection and analysis, and properly reporting instrument parameters. *Applied Surface Science Advances* **2024,** *19*, 100534.
45. Chang, H.-Y.; Lin, W.-C.; Chu, P.-C.; Wang, Y.-K.; Sogo, M.; Iida, S.-i.; Peng, C.-J.; Miyayama, T., X-ray photoelectron spectroscopy equipped with gas cluster ion beams for evaluation of the sputtering behavior of various nanomaterials. *ACS Applied Nano Materials* **2022,** *5* (3), 4260-4268.
46. Moon, S.; Park, J.; Lee, H.; Yang, J. W.; Yun, J.; Park, Y. S.; Lee, J.; Im, H.; Jang, H. W.; Yang, W., et al., Bi2S3-Cu3BiS3 Mixed Phase Interlayer for High-Performance Cu3BiS3-Photocathode for 2.33% Unassisted Solar Water Splitting Efficiency. *Advanced Science* **2023,** *10* (6), 2206286.
47. Shukla, S.; Prabhakar, R. R.; Li, H.; Kim, R. S.; Chen, W.; Beaudelot, J.; D'Haen, J.; Santos, D. R.; Vereecken, P. M.; Rignanese, G.-M., et al., Origin of photoelectrochemical CO2 reduction on bare Cu(In,Ga)S2 (CIGS) thin films in aqueous media without co-catalysts. *EES Catalysis* **2025**.
48. Liu, Y.; Xia, M.; Ren, D.; Nussbaum, S.; Yum, J.-H.; Grätzel, M.; Guijarro, N.; Sivula, K., Photoelectrochemical CO2 Reduction at a Direct CuInGaS2/Electrolyte Junction. *ACS Energy Letters* **2023,** *8* (4), 1645-1651.
49. Guijarro, N.; Prévot, M. S.; Johnson, M.; Yu, X.; Bourée, W. S.; Jeanbourquin, X. A.; Bornoz, P.; Le Formal, F.; Sivula, K., CuInGaS2 photocathodes treated with SbX3 (X = Cl, I): the effect of the halide on solar water splitting performance. *Journal of Physics D: Applied Physics* **2017,** *50* (4), 044003.
50. Chen, S.; Wang, X.; Chen, X.; Zhao, Y.; Dai, G.; Yang, J.; Tang, R.; Chen, T.; Hu, P.; Li, J., Self-Regulated Growth of Large-Grain Sb2S3 Thin Films for High-Efficiency Solar Cells. *Advanced Functional Materials* **2024,** *34* (38), 2402978.
51. Yuan, S.; Deng, H.; Dong, D.; Yang, X.; Qiao, K.; Hu, C.; Song, H.; Song, H.; He, Z.; Tang, J., Efficient planar antimony sulfide thin film photovoltaics with large grain and preferential growth. *Solar Energy Materials and Solar Cells* **2016,** *157*, 887-893.
52. Dimitrievska, M.; Xie, H.; Fairbrother, A.; Fontané, X.; Gurieva, G.; Saucedo, E.; Pérez-Rodríguez, A.; Schorr, S.; Izquierdo-Roca, V., Multiwavelength excitation Raman scattering of Cu2ZnSn(SxSe1−x)4 ($0 \le x \le 1$) polycrystalline thin films: Vibrational properties of sulfoselenide solid solutions. *Applied Physics Letters* **2014,** *105* (3).

53. Gong, Y.; Qiu, R.; Niu, C.; Fu, J.; Jedlicka, E.; Giridharagopal, R.; Zhu, Q.; Zhou, Y.; Yan, W.; Yu, S., et al., Ag Incorporation with Controlled Grain Growth Enables 12.5% Efficient Kesterite Solar Cell with Open Circuit Voltage Reached 64.2% Shockley–Queisser Limit. *Advanced Functional Materials* **2021,** *31* (24), 2101927.
54. Darling, R. M.; Shiau, H.-S.; Weber, A. Z.; Perry, M. L., The Relationship between Shunt Currents and Edge Corrosion in Flow Batteries. *Journal of The Electrochemical Society* **2017,** *164* (11), E3081.
55. Samu, G. F.; Janáky, C., Photocorrosion at Irradiated Perovskite/Electrolyte Interfaces. *Journal of the American Chemical Society* **2020,** *142* (52), 21595-21614.
56. Kato, T.; Handa, A.; Yagioka, T.; Matsuura, T.; Yamamoto, K.; Higashi, S.; Wu, J. L.; Tai, K. F.; Hiroi, H.; Yoshiyama, T., et al., Enhanced Efficiency of Cd-Free Cu(In,Ga)(Se,S)2 Minimodule Via (Zn,Mg)O Second Buffer Layer and Alkali Metal Post-Treatment. *IEEE Journal of Photovoltaics* **2017,** *7* (6), 1773-1780.
57. Cho, J. W.; Ismail, A.; Park, S. J.; Kim, W.; Yoon, S.; Min, B. K., Synthesis of Cu2ZnSnS4 Thin Films by a Precursor Solution Paste for Thin Film Solar Cell Applications. *ACS Applied Materials & Interfaces* **2013,** *5* (10), 4162-4165.
58. Ou, K.-L.; Fan, J.-C.; Chen, J.-K.; Huang, C.-C.; Chen, L.-Y.; Ho, J.-H.; Chang, J.-Y., Hot-injection synthesis of monodispersed Cu2ZnSn(SxSe1−x)4 nanocrystals: tunable composition and optical properties. *Journal of Materials Chemistry* **2012,** *22* (29), 14667-14673.
59. Bär, M.; Schubert, B.-A.; Marsen, B.; Wilks, R. G.; Pookpanratana, S.; Blum, M.; Krause, S.; Unold, T.; Yang, W.; Weinhardt, L., et al., Cliff-like conduction band offset and KCN-induced recombination barrier enhancement at the CdS/Cu2ZnSnS4 thin-film solar cell heterojunction. *Applied Physics Letters* **2011,** *99* (22), 222105.
60. Zhang, S. B.; Wei, S.-H.; Zunger, A.; Katayama-Yoshida, H., Defect physics of the $CuInSe_2$ chalcopyrite semiconductor. *Physical Review B* **1998,** *57* (16), 9642-9656.
61. Baranowski, L. L.; Zawadzki, P.; Lany, S.; Toberer, E. S.; Zakutayev, A., A review of defects and disorder in multinary tetrahedrally bonded semiconductors. *Semiconductor Science and Technology* **2016,** *31* (12), 123004.
62. Meyer, B. K.; Polity, A.; Reppin, D.; Becker, M.; Hering, P.; Klar, P. J.; Sander, T.; Reindl, C.; Benz, J.; Eickhoff, M., et al., Binary copper oxide semiconductors: From materials towards devices. *physica status solidi (b)* **2012,** *249* (8), 1487-1509.
63. DeAngelis, A. D.; Kemp, K. C.; Gaillard, N.; Kim, K. S., Antimony(III) Sulfide Thin Films as a Photoanode Material in Photocatalytic Water Splitting. *ACS Applied Materials & Interfaces* **2016,** *8* (13), 8445-8451.
64. Pantelides, S. T., The electronic structure of impurities and other point defects in semiconductors. *Reviews of Modern Physics* **1978,** *50* (4), 797.
65. Barthwal, S.; Singh, S.; Chauhan, A. K.; Prabhu, N. S.; Prabhudessai, A. G.; Ramesh, K., A comprehensive insight into deep-level defect engineering in antimony chalcogenide solar cells. *Materials Advances* **2023,** *4* (23), 5998-6030.
66. Wang, X.; Kavanagh, S. R.; Walsh, A., Sulfur Vacancies Limit the Open-Circuit Voltage of Sb2S3 Solar Cells. *ACS Energy Letters* **2024,** *10* (1), 161-167.
67. Zhao, R.; Yang, X.; Shi, H.; Du, M.-H., Intrinsic and complex defect engineering of quasi-one-dimensional ribbons Sb2S3 for photovoltaics performance. *Physical Review Materials* **2021,** *5* (5), 054605.
68. Kudo, A.; Miseki, Y., Heterogeneous photocatalyst materials for water splitting. *Chemical Society Reviews* **2009,** *38* (1), 253-278.
69. Liu, Y.; Bouri, M.; Yao, L.; Xia, M.; Mensi, M.; Grätzel, M.; Sivula, K.; Aschauer, U.; Guijarro, N., Identifying Reactive Sites and Surface Traps in Chalcopyrite Photocathodes. *Angewandte Chemie International Edition* **2021,** *60* (44), 23651-23655.
70. Smith, W. A.; Sharp, I. D.; Strandwitz, N. C.; Bisquert, J., Interfacial band-edge energetics for solar fuels production. *Energy & Environmental Science* **2015,** *8* (10), 2851-2862.

71. Shi, L.; Yin, Y.; Wang, S.; Sun, H., Rational Catalyst Design for N2 Reduction under Ambient Conditions: Strategies toward Enhanced Conversion Efficiency. *ACS Catalysis* **2020,** *10* (12), 6870-6899.
72. Nasir, J. A.; ur Rehman, Z.; Shah, S. N. A.; Khan, A.; Butler, I. S.; Catlow, C. R. A., Recent developments and perspectives in CdS-based photocatalysts for water splitting. *Journal of Materials Chemistry A* **2020,** *8* (40), 20752-20780.
73. Zi, W.; Mu, F.; Lu, X.; Liu, Z.; Pang, X.; Yu, Z.; Li, Y.; Zhao, Z.; Lei, B.; Cheng, N., Sputtering Al2O3 as an effective interface layer to improve open-circuit voltage and device performance of Sb2Se3 thin-film solar cells. *Materials Science in Semiconductor Processing* **2023,** *153*, 107185.
74. Sharma, V.; Dakshinamurthy, A. C.; Pandey, B.; Roy, S. C.; Sudakar, C., Effect of oxygen nonstoichiometry on the photoelectrochemical performance of oxide-nanorod based TiO2/Sb2S3 and ZnO/Sb2S3 heterostructured photoanodes. *Nano Express* **2020,** *1* (3), 030038.
75. Lee, Y. S.; Heo, J.; Siah, S. C.; Mailoa, J. P.; Brandt, R. E.; Kim, S. B.; Gordon, R. G.; Buonassisi, T., Ultrathin amorphous zinc-tin-oxide buffer layer for enhancing heterojunction interface quality in metal-oxide solar cells. *Energy & Environmental Science* **2013,** *6* (7), 2112-2118.
76. Chandrasekharan, N.; Kamat, P. V., Improving the Photoelectrochemical Performance of Nanostructured TiO2 Films by Adsorption of Gold Nanoparticles. *The Journal of Physical Chemistry B* **2000,** *104* (46), 10851-10857.
77. Zhou, H.; Chen, Q.; Li, G.; Luo, S.; Song, T.-b.; Duan, H.-S.; Hong, Z.; You, J.; Liu, Y.; Yang, Y., Interface engineering of highly efficient perovskite solar cells. *Science* **2014,** *345* (6196), 542-546.
78. Marshall, K. P.; Walton, R. I.; Hatton, R. A., Tin perovskite/fullerene planar layer photovoltaics: improving the efficiency and stability of lead-free devices. *Journal of materials chemistry A* **2015,** *3* (21), 11631-11640.
79. Bampoulis, P.; van Bremen, R.; Yao, Q.; Poelsema, B.; Zandvliet, H. J.; Sotthewes, K., Defect dominated charge transport and fermi level pinning in MoS2/metal contacts. *ACS applied materials & interfaces* **2017,** *9* (22), 19278-19286.
80. Bae, S.; Moehl, T.; Service, E.; Kim, M.; Adams, P.; Wang, Z.; Choi, Y.; Ryu, J.; Tilley, S. D., A hole-selective hybrid TiO2 layer for stable and low-cost photoanodes in solar water oxidation. *Nature Communications* **2024,** *15* (1), 9439.
81. Liu, Z.; Sun, B.; Liu, X.; Han, J.; Ye, H.; Tu, Y.; Chen, C.; Shi, T.; Tang, Z.; Liao, G., 15% efficient carbon based planar-heterojunction perovskite solar cells using a TiO2/SnO2 bilayer as the electron transport layer. *Journal of Materials Chemistry A* **2018,** *6* (17), 7409-7419.
82. Yu, X.; Raifuku, I.; Kawanishi, H.; Uraoka, Y., TiO2/SnO2 electron transport layer by electron beam deposition for perovskite solar cell application. *Japanese Journal of Applied Physics* **2025,** *64* (3), 030908.
83. de la Fuente, B.; Khurana, D. A.; Vereecken, P. M.; Hubin, A.; Hauffman, T., Nano-TiO2/TiN Systems for Electrocatalysis: Mapping the Changes in Energy Band Diagram across the Semiconductor|Current Collector Interface and the Study of Effects of TiO2 Electrochemical Reduction Using UV Photoelectron Spectroscopy. *ACS Applied Materials & Interfaces* **2024,** *16* (37), 49926-49934.
84. Chen, Y.; Meng, Q.; Zhang, L.; Han, C.; Gao, H.; Zhang, Y.; Yan, H., SnO2-based electron transporting layer materials for perovskite solar cells: A review of recent progress. *Journal of Energy Chemistry* **2019,** *35*, 144-167.